MATERIALS SCIENCE

Fully circular shapable transparent paperboard with closed-loop recyclability and marine biodegradability across shallow to deep sea

Noriyuki Isobe[1,2]*, Keiko Tanaka[3], Shun'ichi Ishii[3], Yasuhiro Shimane[3], Satoshi Okada[3], Kazuho Daicho[2], Wataru Sakuma[2], Kojiro Uetani[4], Toshihiro Yoshimura[1], Katsunori Kimoto[5], Satoshi Kimura[6], Tsuguyuki Saito[2], Ryota Nakajima[5], Masashi Tsuchiya[5], Tetsuro Ikuta[5], Shinsuke Kawagucci[5], Tadahisa Iwata[2], Hidetaka Nomaki[3]

To mitigate marine pollution from single-use plastics, it is crucial to transition to next-generation commodity materials that are derived from biomass and are recyclable and marine biodegradable even at abyssal depths in case of the accidental release to the ocean. Here, we develop an optically transparent millimeter-thick paperboard called transparent paperboard (tPB) through dissolution and coagulation of cellulose. The tPB is made entirely of pristine cellulose and compositionally identical to paper. A cup-shaped tPB can hold just-boiled water without an internal film coating because of its high wet tensile properties and anisotropic thermal properties. In addition, the spent tPB is material recyclable in a closed system, where all chemicals and water are also recyclable. Furthermore, the marine biodegradability of tPB across shallow to abyssal depths is confirmed by on-site degradation tests and metagenomic analyses. Hence, tPB is expected to serve as a key fully circular commodity material in sustainable societies of the future.

INTRODUCTION

Annually, 0.5 to 13 million metric tons of plastic waste are assumed to end up in the ocean (*1*–*4*). One fate of discharged plastic debris is that it remains on deep-sea floors (*5*, *6*). A recent study (*7*) found that the plastic debris that drifts offshore is trapped in a gyre ~500 km away from land and ultimately sinks and accumulates on the deep-sea floor with a high density of more than 4500 items/km^2; most of these materials are single-use plastics, such as food packaging or plastic bags. To mitigate this problem, the strict management of plastic debris is urgently needed (*8*, *9*), in which all plastics should be collected after use and recycled to achieve a circular economy. However, a previous study has shown that strong winds and heavy rainfall induce the unavoidable accidental release of a large amount of plastic waste from land through rivers, making the complete recovery of plastic debris even more difficult (*10*). By considering these problems, a next-generation commodity plastic needs to meet the three following criteria (*11*): (i) to originate from biomass to reduce fossil fuel use, (ii) to be recyclable to achieve a circular economy, and (iii) to be marine biodegradable across shallow to abyssal depths in case of accidental release.

Paper is a long-standing versatile sheet material made from cellulose originating from plant cell walls. Paper thickness is an important parameter for its application. For printing and writing purposes, paper is generally thin, with thicknesses of 0.05 to 0.1 mm. Thick paper, with a grammage above 250 g/m^2 or a thickness greater than ~0.3 mm, is referred to as paperboard (PB) (*12*); PB is used for packaging and containers because of its integrity and foldability. In response to increasing environmental concerns, PB has been focused on as a replacement for conventional petroleum-based plastics because of its biomass origin and recyclability (*13*). However, one of the drawbacks of PB is its opacity: Transparent packaging is impossible with conventional PB because of the light scattering induced by the macrofibers in wood pulps (*14*). Transparent packaging is aesthetically indispensable for commercial success in certain applications, such as food packaging or containers (*15*); thus, the use of petroleum-based transparent plastics, such as polyethylene terephthalate, is unavoidable, thereby necessitating the development of transparent PB, which is regarded as technically impossible (*16*).

Regenerated cellulose is another class of fully cellulose-based materials. Cellulose is solubilized into specific solvents (*17*–*21*) and solidified by immersion into nonsolvents, followed by thorough washing and drying. A transparent cellulose sheet with thicknesses of 0.02 to 0.04 mm, called cellophane, is produced on a commercial scale using this process. However, increasing the thickness of cellophane is limited because of the regeneration step: Solidification is driven by the diffusion of nonsolvents into the cellulose solution; thus, homogeneous and complete solidification is not possible at large thicknesses.

In this context, we develop a long-sought fully cellulose-based transparent PB-like material based on regenerated cellulose, denoted as transparent PB (tPB). This was achieved by the simple drying of thick, bulky, and shapable cellulose hydrogel prepared using aqueous lithium bromide (LiBr) solution as the solvent, where cellulose solution solidifies without the introduction of nonsolvents: Cellulose dissolves upon heating and solidifies upon cooling (*22*–*24*). With this process, tPB emerges as a transparent, three-dimensional thick material made solely from

[1]Research Institute for Marine Resources Utilization (MRU), Japan Agency for Marine-Earth Science and Technology (JAMSTEC), 2-15 Natsushima-cho, Yokosuka 237-0061, Kanagawa, Japan. [2]Department of Biomaterial Sciences, Graduate School of Agricultural and Life Sciences, The University of Tokyo, 1-1-1 Yayoi, Bunkyo-ku, Tokyo 113-8657, Japan. [3]Institute for Extra-cutting-edge Science and Technology Avant-garde Research (X-STAR), Japan Agency for Marine-Earth Science and Technology (JAMSTEC), 2-15 Natsushima-cho, Yokosuka 237-0061, Kanagawa, Japan. [4]Department of Industrial Chemistry, Faculty of Engineering, Tokyo University of Science, 6-3-1 Niijuku, Katsushika-ku, Tokyo 125-8585, Japan. [5]Research Institute for Global Change, Japan Agency for Marine-Earth Science and Technology (JAMSTEC), 2-15 Natsushima-cho, Yokosuka 237-0061, Kanagawa, Japan. [6]Technology Advancement Center, Graduate School of Agricultural and Life Sciences, The University of Tokyo, Tokyo 113-8657, Japan.
*Corresponding author. Email: isoben@jamstec.go.jp

pristine cellulose, capable of taking various forms ranging from millimeter-thick board to cup or straw shapes. To date, transparent materials composed entirely of pristine cellulose have been limited to two-dimensional thin films with thicknesses below 0.1 mm (*25*–*28*). In contrast, while composites with resins can achieve thickness and transparency (*29*, *30*), they are no longer purely cellulose based, thereby forfeiting the biodegradability and material recyclability inherent to purely cellulose-based material. There are four aims of this study: (i) to clarify the structure-property relationships, (ii) to demonstrate its three-dimensionally shapable nature, (iii) to examine the closed-loop recyclability, and (iv) to validate the marine biodegradability of tPB across shallow to abyssal depths and the corresponding mechanisms. Through these studies, we show that tPB meets the criteria for a next-generation commodity material: biobased, closed-loop recyclable, and marine biodegradable across shallow to abyssal depths.

RESULTS

Fabrication of tPB

The tPBs with thicknesses of 0.2 to 1.5 mm were successfully prepared by drying centimeter-thick cellulose hydrogel (Fig. 1A). The hydrogel was prepared by dissolution of cellulose powder or textile in aq. LiBr solution by heating, coagulation by cooling to room temperature, and subsequent washing with water. The obtained smartphone-sized tPB (138 mm by 67 mm) with a thickness of 0.7 mm showed high transparency: One could see a ship ~150 m away through the tPB (Fig. 1A). Even upon an increase in thickness up to 1.5 mm, the tPB retained visibility while showing slight opacity (inset in Fig. 1A). The absence of impurities from the manufacturing process such as residual LiBr was confirmed by inductively coupled plasma mass spectrometry (ICP-MS) (table S1). The successful preparation of such a thick cellulose plate was not feasible with conventional regenerated cellulose because of inhomogeneous gelation, as shown in fig. S1.

Here, we examined the potential of tPB as a next-generation commodity material, as schematized in Fig. 1B. The origin of cellulose in this study was cotton linter, which was the fine fiber covering cotton seeds that was too short to be spun into fibers. As a starting material, two commercially available cotton linter products were chosen: microcrystalline cellulose powder (MCC) and nonwoven cellulose textile (*31*). First, the structure-property relationships of tPBs (tPB_{MCC} and tPB_{tex}, respectively) were elucidated. Then, to demonstrate its potential application, the tPB was shaped into a cup and straw, and its practical usability was evaluated. Furthermore, closed-loop recycling of the solvent and material was tested to show the fully circular nature of tPB. Last, its marine biodegradability

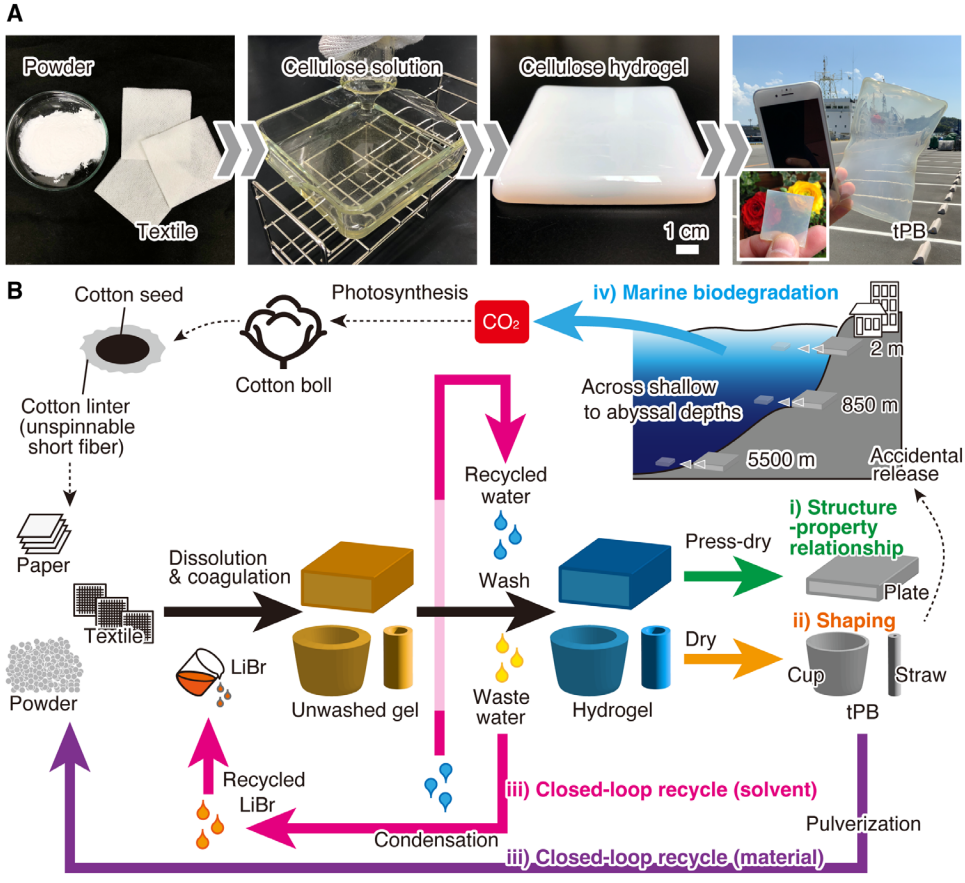

Fig. 1. Fabrication of tPB. (**A**) Preparation scheme of tPB. "Powder" and "Textile" refer to MCC and nonwoven cellulose textile, respectively. A millimeter-thick tPB [the one with the thickness of 0.7 mm is shown with a smartphone (138 mm by 67 mm), and 1.5 mm is shown in the inset] was prepared by drying a centimeter-thick cellulose hydrogel produced by cellulose dissolution and coagulation in aqueous LiBr solution. (**B**) Overview of the fully circular nature of tPB in this study.

across shallow to abyssal depths was examined by on-site degradation tests and metagenomic analyses.

Structure-property relationships of tPB

The transparency of tPB (Fig. 1A) was evaluated by the total transmission of light (T_t) and haze (Fig. 2A). With increasing thickness of tPB_{MCC}, T_t decreased exponentially (*32*, *33*) from 87% at a 0.3-mm thickness to 64% at a 1.5-mm thickness, and haze increased exponentially (*28*, *29*) from 22% at a 0.3-mm thickness to 49% at a 1.5-mm thickness. Although the optical properties were not as high as those of cellulose nanofiber films (*25*, *34*, *35*) and plate (*36*) [compare less than 2% of haze at a thickness of 0.015 mm (*35*) and 8% of haze at a thickness of 1.12 mm (*36*)], clear transparency was guaranteed, as demonstrated in Fig. 1A. The exponential increase in haze was well fitted with the model of a transparent plate homogeneously embedded with light-scattering colloids (*37*). This phenomenon indicated that unlike glass or poly(methylmethacrylate), light-scattering agents inducing the opacity were present inside tPB and were homogeneously distributed in the thickness direction. As such light-scattering agents, residual pores are likely because the pore volume was estimated to be ~16%, as calculated from the bulk (1.29 ± 0.03 g/cm^3) and true (1.530 ± 0.007 g/cm^3) densities. The pore size should be on the submicrometer scale, as no visible pores were observed by micro–x-ray tomography with a voxel size of 1 μm (movie S1). In addition, tPB showed a slightly bluish color (Fig. 1A). This was due to the lower transmittance in the blue-light spectral region, as shown in fig. S2. The optical properties of tPB_{tex} were in accordance with those of tPB_{MCC} (Fig. 2A).

Bending stress, a crucial property for the practical use of thick plate-like materials, was evaluated through the three-point bending test (Fig. 2B and table S2). From the flexural stress-strain (S-S) curves, Young's modulus of tPB_{MCC} was found to be as high as that of conventional PB but twice as high as that of conventional hard plastic [polycarbonate (PC)]. After reaching the highest flexural

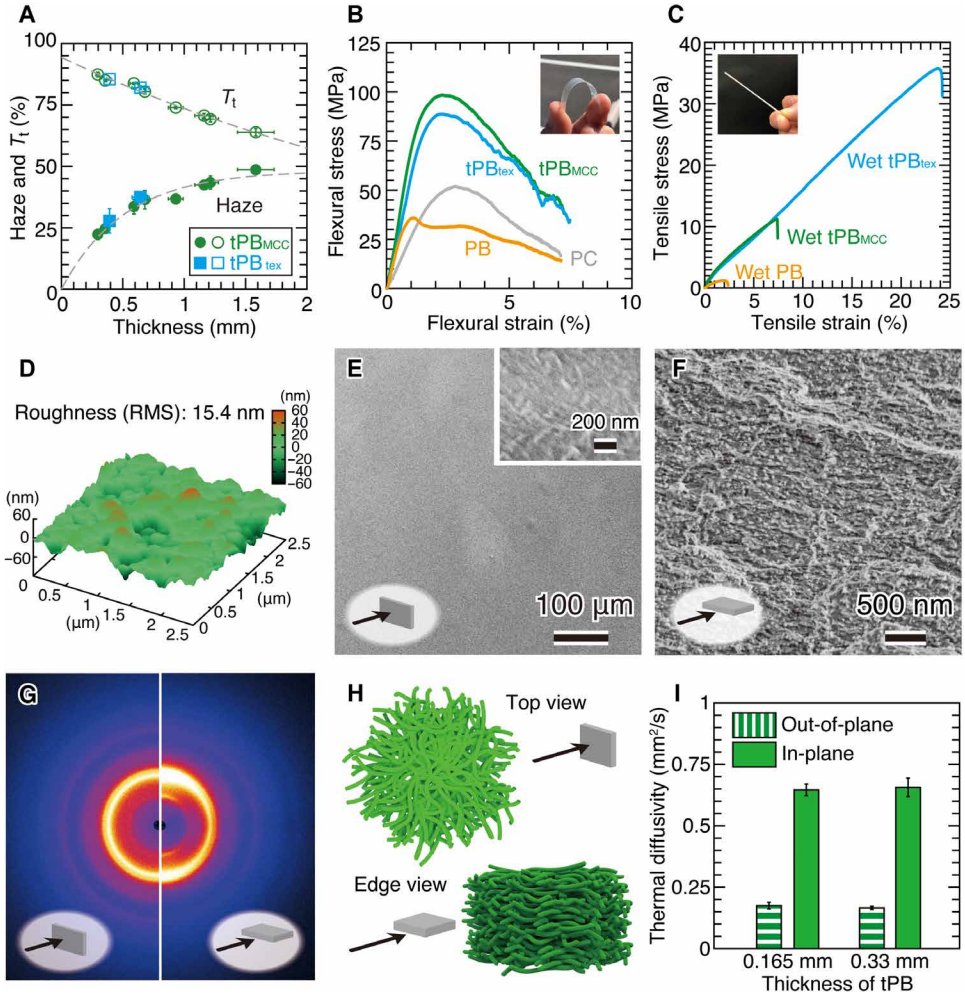

Fig. 2. Structure-property relationships of tPB. (**A**) Haze and total transmission (T_t) of tPB_{MCC} and tPB_{tex}. The dotted line is a regression curve based on references (*32*, *37*). (**B**) Flexural stress-strain curves of PB, PC, tPB_{MCC}, and tPB_{tex} with thicknesses of 0.5 mm. The bending test stopped at the strain of 7%, because the sample specimen started to slip, as seen in the abrupt decrease in stress. A manually bent tPB_{MCC} is shown in the inset. (**C**) Wet tensile stress-strain curves of PB, tPB_{MCC}, and tPB_{tex}. (**D**) AFM image of tPB_{MCC}. (**E**) Surface SEM image of tPB_{MCC} shown with higher magnification in the inset. (**F**) Cross-sectional SEM image of tPB_{MCC}. (**G**) Through-view (left) and edge-view (right) WAXD image of tPB_{MCC}. (**H**) Schematic representation of tPB and (**I**) thermal diffusivity of tPB_{MCC} with different thicknesses. The 0.165-mm–thick tPB_{MCC} was prepared by polishing 0.33-mm–thick tPB_{MCC} with sandpaper.

modulus of ~100 MPa, tPB_{MCC} showed yielding behavior without fracturing, as seen in the inset of Fig. 2B, and exerted 50 MPa at strains of 7%. In contrast, conventional PB was broken or folded at 1% strain and exerted almost no stress at 6% strain. Therefore, tPB was determined to be a material that combined the hardness of conventional PB and the ductility of conventional plastics.

Another key mechanical property is wet strength, which is generally considered as a drawback of fully cellulosic materials (*38*). According to the standard protocol (*38*), tPB was immersed in water for more than 72 hours and subjected to the tensile test (Fig. 2C and table S3). Although the wet sample specimen of tPB contained 30 wt % water, it stood alone without drooping, as shown in the inset of Fig. 2C. Even in this fully hydrated state, tPB did not break until it reached tensile shear strains of 7% (tPB_{MCC}) and 24% (tPB_{tex}), and the fracture stress was 5 times (tPB_{MCC}) and 15 times (tPB_{tex}) higher than that of conventional PB. The high wet strength of tPB stemmed from the continuous fibrous network formed in the undried cellulose hydrogel (fig. S3) (*22*, *23*). The higher wet mechanical property of tPB_{tex} compared to tPB_{MCC} was due to the difference in molecular weight [112,000 g/mol for nonwoven textile (*39*) and 32,900 g/mol for MCC (*40*)].

The clear transparency of tPB arose from the smooth surface. The atomic force microscopy (AFM) image showed that the roughness of tPB_{MCC} was on the nanometer scale (Fig. 2D). This smoothness was corroborated by the surface scanning electron microscopy (SEM) images of tPB_{MCC} (Fig. 2E). The higher magnification (inset in Fig. 2E) showed that the smooth surface was made of a coalesced fibrous network. The cross-sectional SEM image showed a stacked fibrous network (Fig. 2F), indicating that the fibrous network formed in the undried cellulose hydrogel (fig. S3) was stacked together by unidirectional compression during drying. The wide-angle x-ray diffraction (WAXD) (Fig. 2G and fig. S4) and small-angle x-ray scattering (SAXS) (fig. S5) patterns showed that the nanofibrous structure was oriented parallel to the in-plane direction, as schematized in Fig. 2H. This anisotropic structure resulted in thermal diffusivity anisotropy (Fig. 2I): The out-of-plane direction showed 3.7 times lower thermal diffusivity than the in-plane direction. The thermal diffusivity was almost identical before (0.33-mm-thick) and after (0.165-mm-thick) polishing, demonstrating that the structural inhomogeneity inside tPB was negligibly small.

Shaping of tPB

To explore the potential applications of tPB, a cup- or straw-shaped tPB_{tex} was prepared (fig. S7). The cup- or straw-shaped tPB_{tex} exhibited transparency (haze of 32% at a 0.45-mm thickness) similar to plate-shaped tPB_{tex}, allowing one to see the color of the beverage inside (Fig. 3, A and B). This transparency was achieved without hot-pressing, necessary for plate-shaped tPB preparation. Because of the difference in the mode of drying, the straw-shaped tPB_{tex} demonstrated greater ductility when compared to plate-shaped tPB_{tex} (fig. S8).

The abovementioned high wet strength rendered the cup-shaped tPB_{tex} durable upon being filled with water: There was no leakage of water (Fig. 3, A and B, and fig. S9) even without any plastic film coating on the inner surface, which was mandatory for conventional PB cups, offering an eco-friendly alternative to conventional single-use paper and plastic cups. Even after 3 hours of retention of water inside the cup, only 1.2 wt % of water permeated through the cup

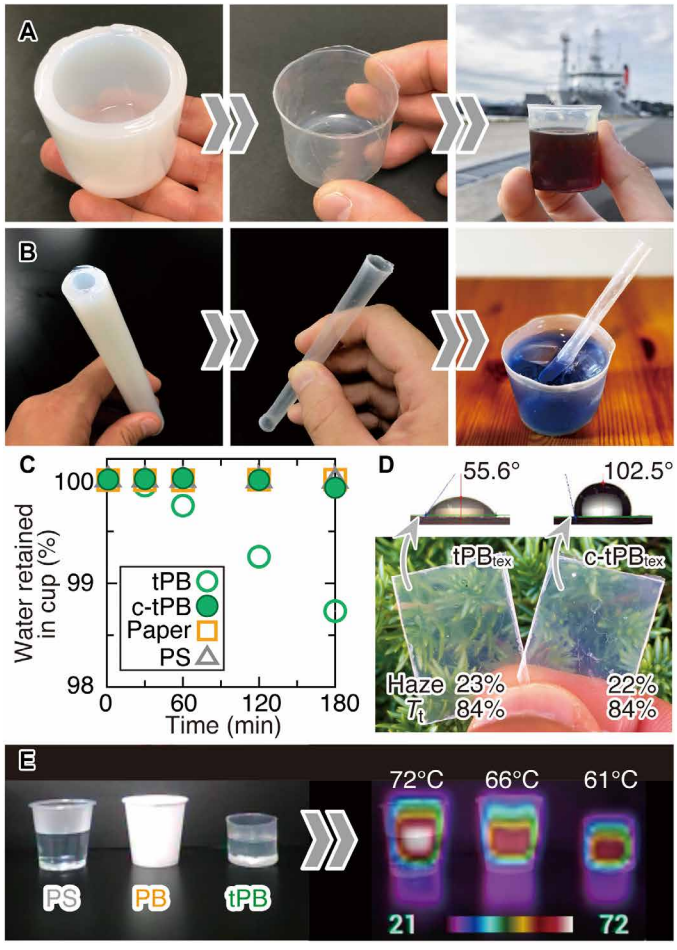

Fig. 3. Shapable nature of tPB. (**A**) Preparation scheme and appearance of cup-shaped tPB_{tex}. The liquid-filled shaped tPB_{tex} was photographed within 30 min from filling of hot coffee. (**B**) Preparation protocol and appearance of straw-shaped tPB_{tex}. The liquid-filled shaped tPB_{tex} was photographed within 30 min from filling of iced butterfly pea tea. (**C**) Time-course retention of water filled in the cups sealed with a film on top as in fig. S6 to avoid evaporation from the water surface. (**D**) Contact angle measurement and appearance of tPB_{tex} and c-tPB_{tex}. Coating by fatty acid salt was performed using aluminum distearate. The values with the respective errors are shown in table S4. (**E**) Thermography of cups made of polystyrene (PS), PB, and tPB. Just-boiled water was poured into the cups, and the cups were analyzed within 1 min.

wall and evaporated from the cup wall surface (tPB_{tex} in Fig. 3C). This minor water permeation was effectively prevented by applying a surface coating with plant-derived fatty acid salt. The coated tPB_{tex} (c-tPB_{tex}) repelled a water droplet while retaining transparency (Fig. 3D). The c-tPB_{tex} cup exhibited no water leakage and maintained water retention capabilities comparable to a commercial paper cup lined with a plastic film coating on the inner surface and a polystyrene (PS) cup (Fig. 3C), expanding tPB's application to containers with extended shelf lives. It should be noted that the coating was exclusively applied to the inner surface of the cup (fig. S10) and the estimated thickness of the coating layer was ~5 to 10 μm: 7.1 μm based on the weight increase and 5.0 to 6.5 μm based on the aluminum content measured by ICP-MS. In addition, this coating demonstrated excellent durability under repetitive wetting and

drying cycles (fig. S11). Furthermore, the abovementioned anisotropic thermal diffusivity (Fig. 2I) contributed to the thermal insulating nature of the cup-shaped tPB_{tex} (Fig. 3E).

Closed-loop recyclability of tPBs

Closed-loop recyclability was evaluated using tPB_{tex} (Fig. 4). First, the recycling of the spent solvent was established. The wastewater from the washing step of cellulose gel is a dilute aqueous LiBr solution containing by-products such as thermally decomposed carbohydrates. Through evaporative condensation (fig. S12), the LiBr concentration was increased to 60 wt %. The evaporated water was recovered by cooling and reused as washing water. By-products were removed by activated carbon (*41*), and the treated LiBr solution was then used in the preparation of tPB_{tex} (Fig. 4A). The solvent-recycled tPB_{tex} showed a similar, and even clearer, appearance compared to the original tPB_{tex}, indicating the success of solvent recycling.

Second, the material recycling of tPB_{tex} was attempted. The tPB_{tex} was pulverized (fig. S13) and subjected to dissolution by LiBr solution. As indicated by the increase in haze (from 19 to 54%), the material-recycled tPB_{tex} became translucent (Fig. 4A). This increase in haze was likely due to the undissolved fraction contained in tPB_{tex}. However, the T_t of material-recycled tPB_{tex} remained high at 86% (Fig. 4B). As a result, the visibility of colors positioned directly behind the material-recycled tPB_{tex}, which is crucial for packaging application, was maintained.

Third, the combination of solvent and material recycling was tested. The solvent-material–recycled tPB_{tex} was produced from the spent tPB_{tex} using the recycled LiBr solvent. Although the solvent-material–recycled tPB_{tex} exhibited slightly higher translucency (haze: 60%) than material-recycled tPB_{tex} (Fig. 4A), the T_t (83%) remained almost constant compared to the original one (Fig. 4B). Therefore, the visibility of colors behind the tPB was also maintained even in the combination of solvent and material recycling (Fig. 4B).

The mechanical properties of recycled tPB_{tex} (Fig. 4C) were mostly similar, except for the material-recycled tPB_{tex}, which showed a 10% decrease in the maximal flexural stress. The wet tensile strength of material-recycled tPB_{tex} decreased to half that of the original tPB_{tex} (table S2). This inferior mechanical property of material-recycled tPB_{tex} was likely due to the decrease in the molecular weight (Fig. 4D) that occurred during the dissolution process (*22*). However, despite the decrease in the mechanical properties, material-recycled tPB_{tex} showed a 1.5-fold higher maximal flexural stress than PC and a 10-fold higher wet tensile strength than conventional PB (table S3), ensuring the reusability of material-recycled tPB_{tex}.

Last, the upcycling of spent cellulosic materials was attempted. In principle, the production process of tPB can be applied to unexploited cellulose wastes such as worn fabrics, waste papers, and low-value wood. To demonstrate this, filter paper and copying paper were transformed into tPB, denoted as tPB_{FP} and tPB_{CPP}, respectively (Fig. 4, E and F). The haze and T_t of tPB_{FP} and tPB_{CPP} were similar to those of the material-recycled tPB_{tex}, indicating the successful upcycling of cellulose wastes. The decontamination of postconsumer tPB will be a critical issue for its implementation. For large-scale decontamination of inks or adhesives, the well-established industrial deinking process under alkaline conditions, commonly used in paper recycling, should also be applicable to the spent tPB.

Marine biodegradability of tPB across shallow to abyssal depths

In case of undesired accidental release of tPB from the land to the ocean, marine biodegradability across shallow to abyssal depths was verified by on-site degradation tests combined with multimetaomic analyses. This is meaningful because biodegradation at the deep-sea floor is known to be extremely slow (*42*) despite the high accumulation of single-use plastic wastes. On-site degradation was performed at four different sites: one coastal site (PJM), two bathyal sites close to populated areas (BMS and BHT), and one abyssal site (AMN). To avoid physical degradation, such as collision or abrasion, the sample specimen was protected in triplicate (fig. S13, C to O); the seawater exchange was maintained through the open pores. Hence, the degradation rate calculated from the weight loss of the samples (Fig. 5A) was mostly attributed to the biological actions induced by microorganisms (*42*). The degradation rate of tPB at the deep-sea floor ranged from 20 to 50 $\mu g/cm^2$ per day, which was 5 to 11 times slower than that under coastal conditions (225 $\mu g/cm^2$ per day). This difference resulted from the lower activity of microorganisms under cold (2° to 4°C) conditions (*43*). However, the degradation rates on deep-sea floors were substantial because the cup-shaped tPB_{tex} (thickness, 0.2 mm) shown in Fig. 5A would be completely degraded in 300 days at BMS on the basis of the degradation rates.

The degraded tPB surface was largely covered by a biofilm (Fig. 5B). Underneath the biofilm, numerous microbes were present and penetrated the tPB surface. To identify the microbes inhabiting the tPB surface, genome-centric metagenomic analyses were performed for the biofilm formed at BHT. Extracted draft genomes of the seven highly abundant microbes (Fig. 5C and table S5) included two dominant Fibrobacteres bacteria (40% Fibr1 and 18% Fibr2). The metatranscriptomic analysis based on mRNA sequencing clearly revealed that the two Fibrobacteres bacteria decomposed cellulose with oxygen respiration by secreting endoglucanases and β-glucosidases, while an anaerobic *Spirochaeta* bacterium likely decomposed the cellobiose produced by endoglucanases by using a cellobiose phosphorylase (Fig. 5D), indicating that they were involved in tPB digestion. The most dominant microbe, Fibr1, showed a notably high expression of nitrogenase genes (*nif*), implying that the microbe fixed nitrogen under deep-sea conditions. From the whole community gene expression profile, we reconstructed a metabolic network of the dominant seven microbes (Fig. 5E), suggesting that the two Deltaproteobacteria microbes consumed fermentation by-products, such as hydrogen and formate, through sulfate reduction, while relatively inactive Bacteroidetes and Alphaproteobacteria were assumed to play roles in biofilm stability. All these results strongly indicated the biodegradability of tPB with the release of CO_2 in the deep-sea environment, guaranteeing removal even in the deep-sea ecosystem in the case of accidental release to the ocean.

DISCUSSION

The energy consumption during tPB production was compared to that of conventional PB (table S6). To produce plate-shaped tPB, 640 times more energy (4800 GJ/metric ton) was consumed compared to conventional PB (7.5 GJ/metric ton). This high energy input primarily originated from the press-drying (4710 GJ/metric ton), wherein only one postcard-sized sample could be prepared at a time using laboratory-scale electric apparatus. In contrast, cup-shaped tPB consumed only 8.5 GJ/metric ton during the drying step owing

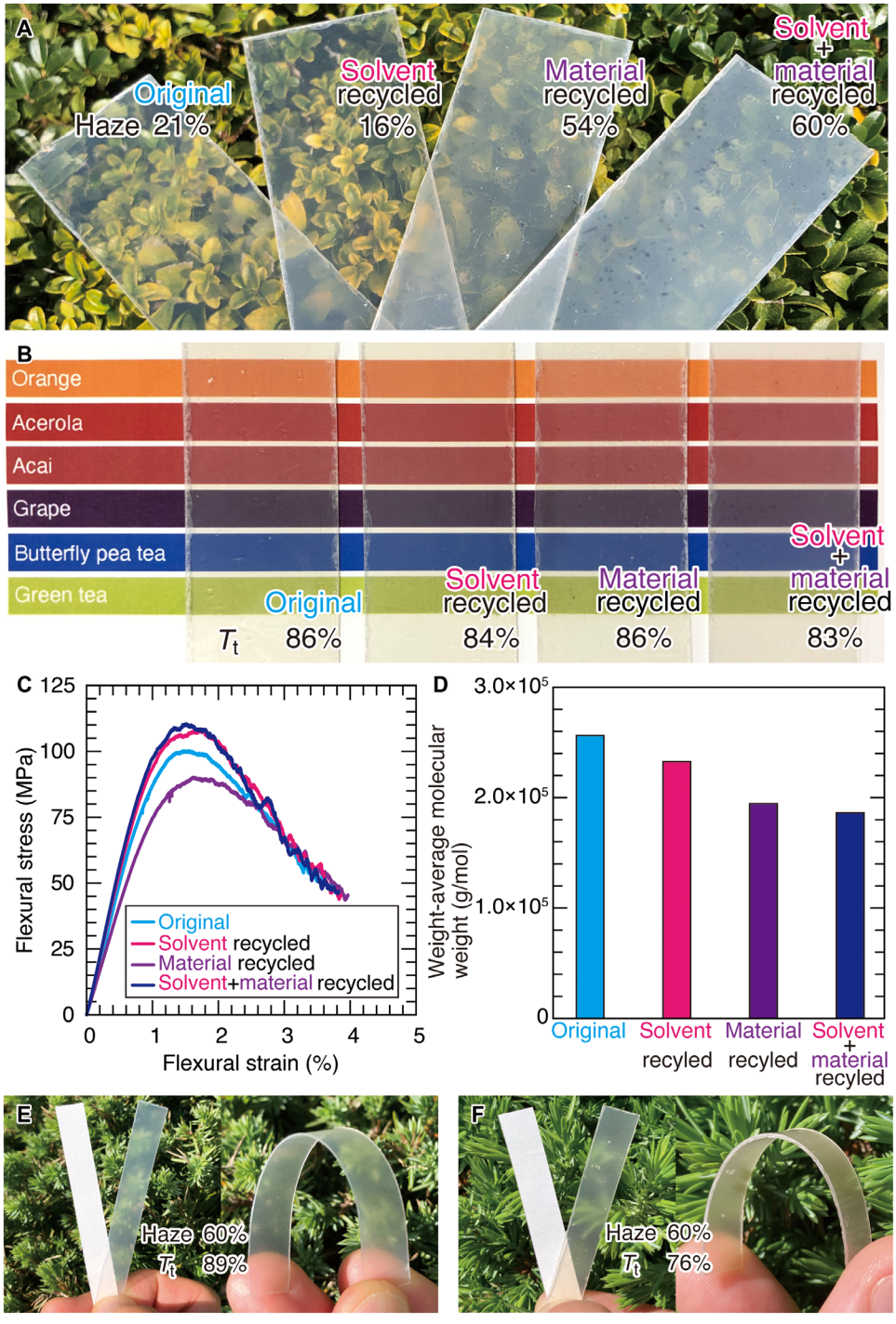

Fig. 4. Closed-loop recyclability. (**A**) tPB_{tex} ("original"), solvent-recycled tPB_{tex}, material-recycled tPB_{tex}, and solvent-material–recycled tPB_{tex} positioned ~10 cm in front of the leaves, shown with the haze values. The values with the respective errors are shown in table S4. (**B**) tPB_{tex} ("original"), solvent-recycled tPB_{tex}, material-recycled tPB_{tex}, and solvent-material–recycled tPB_{tex} positioned in contact with a color paper, featuring the typical colors used in foods and beverages, shown with the T_t values. The values with the respective errors are shown in table S4. (**C**) Flexural stress-strain curves of tPB_{tex} ("original"), solvent-recycled tPB_{tex}, material-recycled tPB_{tex}, and solvent-material-recycled tPB_{tex} with thicknesses of 0.3 mm. Owing to the smaller thickness compared with Fig. 2B (0.5 mm), the flexural stress of tPB_{tex} ("original") showed a higher value than in Fig. 2B. (**D**) M_w of tPB_{tex} ("original"), solvent-recycled tPB_{tex}, material-recycled tPB_{tex}, and solvent-material–recycled tPB_{tex} determined by GPC. It should be noted that M_w was higher than the literature data (*39*, *40*) because of the known overestimation (*86*). (**E**) Whatman no. 2 filter paper on the left and tPB made from the filter paper (tPB_{FP}; thickness, 0.3 mm) on the right. A manually bent tPB_{FP} is shown in the inset. (**F**) Copying paper on the left and tPB made from the copying paper (tPB_{CPP}; thickness, 0.4 mm) on the right. A manually bent tPB_{CPP} is shown in the inset.

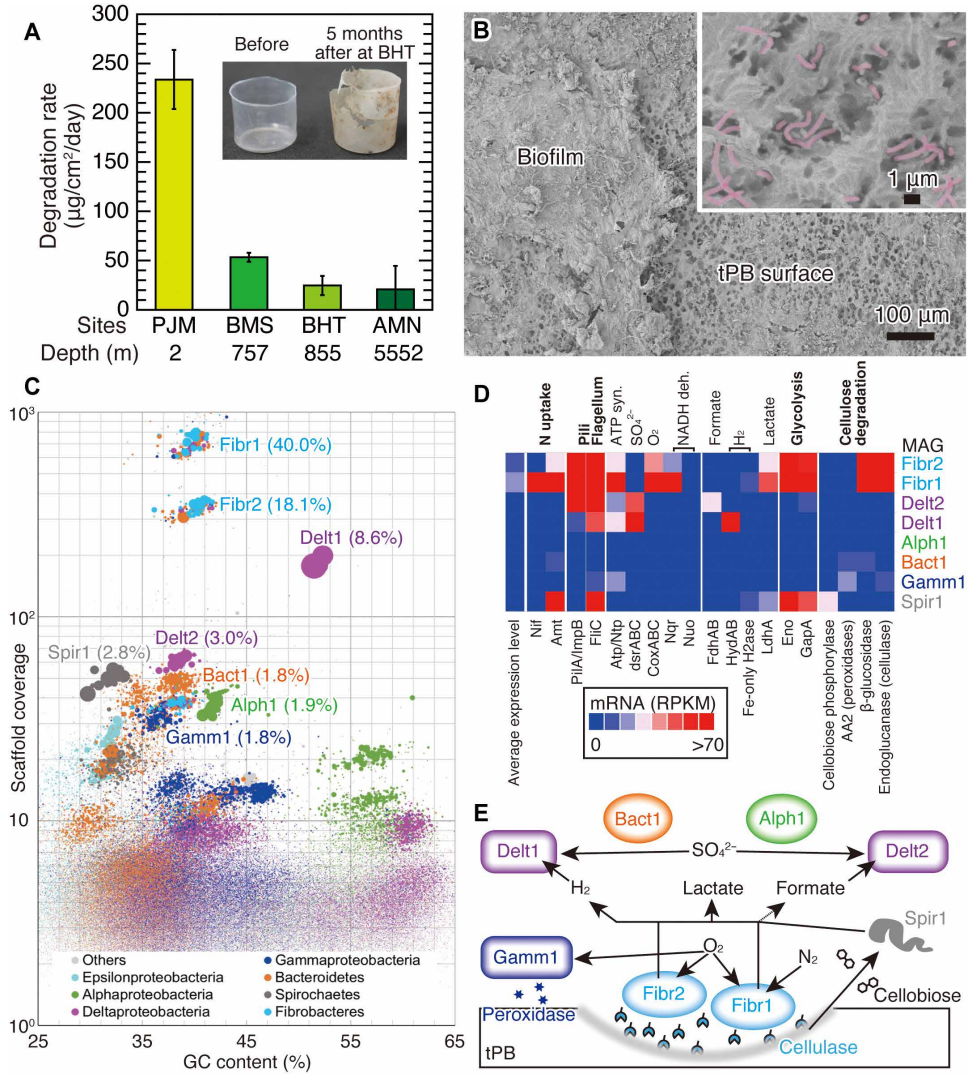

Fig. 5. Marine biodegradability of tPB across all depths. (**A**) Degradation rate of tPB_{MCC} at four different test sites: port of JAMSTEC Yokosuka Headquarters (PJM; depth, 2 m), bathyal seafloor off Misaki Peninsula (BMS; depth, 757 m), bathyal hydrocarbon seepage off Hatsushima Island (BHT; depth, 855 m), and abyssal plain around Minamitorishima Island (AMN; depth, 5552 m). Cup-shaped tPB_{tex} degraded at BHT (855 m) after 5 months of immersion is shown in the inset. (**B**) SEM image of the tPB_{MCC} surface after degradation with BHT (855 m), as detailed in fig. S14 (A and B). Microbes in the inset are colored in pink for clarification. (**C**) Metagenomic assembly of the surface microbiome of tPB_{MCC} degraded at BHT (855 m) to identify MAGs. The MAG names and frequency in percent form are shown near the scaffold clusters. (**D**) Metatranscriptomic analysis based on mRNA sequencing for the MAGs from the tPB_{MCC}-degrading microbiome at BHT. (**E**) Schematic of metabolizing tPB in a deep-sea environment at BHT (855 m).

to the simple air-drying in an oven. The energetic efficiency indicates that the shaping of tPB does not increase and may even lead to a marked decrease in energy consumption during production. Contrastingly, shaping conventional PB requires additional energy input for processes such as punching, folding, and heat sealing. In general, energy consumption during production can be reduced through mass production. To reduce the energy input, modern paper mills use the heat of steam from boilers, which is significantly more energy efficient than heating with electricity (*44*). By using the cooker used in the kraft pulping process of commercial paper mills for the dissolution step in tPB production, the estimated energy consumption during dissolution is 2.7 GJ/metric ton. With this large-scale dissolution, the overall energy consumption for cup-shaped tPB production would decrease to 11.2 GJ/metric ton, which is only 1.5 times higher than that of commercial PB. This estimation suggests that mass-producing tPB with the same energy input as conventional PB would be feasible.

To evaluate the potential environmental benefits of tPB production, a life cycle assessment (LCA) was conducted. For this, we modeled an ideal mass-production process (fig. S15), where large-scale washing is carried out using a counterflow washing method, and wastewater is recovered and recycled using an energy-efficient technique developed to date. Under these ideal mass-production conditions, the greenhouse gas emissions by tPB production would be approximately three times that of conventional PB, three-quarters that of cellophane, and half to two-thirds that of plastic packaging (fig. S16). Therefore, replacing transparent packaging materials with tPB could be environmentally beneficial. In addition, a

technoeconomic perspective was considered by factoring in the cost of dissolving pulp, which is approximately three times higher than that of conventional pulps used for PB. As a result, the estimated price of tPB is projected to be about three times that of commercial PB, demonstrating its economic feasibility. However, optimizing the production process—such as improving the energy-intensive drying stage and developing a continuous manufacturing process (fig. S15)—could further lower production costs, thereby enhancing its market competitiveness.

As suggested by the LCA calculations based on the ideal mass-production process, the repeated use of LiBr is a critical step for the large-scale production of tPB. To address this, the recycling of the solvent (60 wt % aq. LiBr solution) from wastewater (30 wt % aq. LiBr solution) was achieved through the condensation followed by the removal of by-products using activated carbon. Moreover, the water recovered during the condensation was reusable as washing water. Although LiBr solution was widely used to prepare cellulosic materials such as thin films (*45*, *46*), scaffolds for tissue engineering (*23*, *47*), foams (*48*), and aerogels (*49*–*52*), the recycling of the solvent used therein has not been reported to date. Although LiBr solution is stable and nontoxic, it has a corrosive nature. However, the safe manipulation of highly concentrated LiBr solutions on an industrial scale has already been established. This is exemplified by the utilization of metric ton-scale 60 wt % aq. LiBr solution as a working fluid in the absorption heat pump system of air-conditioning, chiller, and refrigerator in industrial plants and large buildings (*53*, *54*). In the absorption heat system, the dilution (from 60 to 40 wt %) and condensation (from 40 to 60 wt %) of aqueous LiBr solution are continuously repeated (*55*, *56*). Consequently, the condensation conducted in this study can be scaled up to a commercial level. In addition, energetically efficient processes without heating such as electrodialysis (*57*) and vacuum membrane distillation (*58*) were already demonstrated in LiBr condensation. Furthermore, a solar-powered cooling system (10-metric ton scale) based on LiBr solution has already been installed in Thailand (*59*). These indicate that tPB production can be transformed into a completely closed process in a cost-effective and environmentally benign manner.

The spent tPB was successfully transformed back into tPB, demonstrating closed-loop recyclability. In each material recycling, the weight-average molecular weight (M_w) decreased by ~18% (fig. S17A). This decrease in M_w was comparable to polyethylene terephthalate, one of the well-known recyclable plastics (*60*). Considering the lower limit of molecular weight required for tPB preparation, it was determined that the maximum amount of material recycling should be limited to three times (fig. S17B). To address this wear-out, the addition of virgin cellulose, commonly used in paper recycling, would prove beneficial.

The tPB exhibited marine biodegradability with a substantial decomposition rate observed from shallow to abyssal depths. It is known that biodegradation speed at the deep-sea floor is extremely slow compared to on land (*61*–*64*). Therefore, the confirmed deep-sea biodegradability in this study is indicative of fast biodegradation in the soils. In addition, the effect of fatty acid salt (aluminum distearate) coating of cup-shaped tPB, as shown in Fig. 3 (C and D), is considered negligible in terms of marine biodegradability. This is attributed to (i) the one-sided and <10-μm thickness of the coating layer, (ii) fatty acid being a natural product that can degrade in the sea (*65*), and (iii) the ubiquity of aluminum in the seawater [3.8 to 6.1 Tg/year of global input to the ocean (*66*, *67*)].

Achieving these advantages—transparency, high mechanical properties, shapability, solvent and material recyclability, and marine biodegradability—is feasible only with tPB. Compressed delignified wood, another class of single-component cellulose material with extraordinary mechanical properties because of the preserved structure of wood cell walls (*68*, *69*), exhibits thinness (less than 100 μm) and haziness (T_t was more than 60% at a thickness of 50 μm) and is not material recyclable. Through the utilization of unexploited cellulose wastes such as worn fabrics, waste papers, and low-value wood, tPB can play a pivotal role in the sustainable circular economy of the future.

MATERIALS AND METHODS

Materials and chemicals

Microcrystalline cellulose powder (Merck, Germany), Bemcot (Asahi KASEI, Japan), and filter paper (Whatman, US) were used as cellulose samples. Lithium bromide, aluminum distearate, ethanol, and cyclohexane were of reagent grade (FUJIFILM Wako Pure Chemical, Japan) and were used without further purification. For the water source during the experiments, we used ultrapure water from a Milli-Q Reference (Merck, Germany). Polycarbonate resin board (Hikari Co., Ltd., Japan) and PB (SEI-830, KOKUYO Co., Ltd., Japan) were used as reference materials for the mechanical analyses.

Sample preparation

Cellulose solution specimens with concentrations of 1 to 5 wt % were prepared as reported (*22*, *23*). A 60 wt % LiBr aqueous solution was heated to desired temperature (155°C for microcrystalline cellulose powder and 115°C for Bemcot and filter paper) for desired time (6 min for microcrystalline cellulose powder and 50 min for Bemcot and filter paper), and a desirable amount of cellulose was added to the heated LiBr aqueous solutions. After complete cellulose dissolution was confirmed by visible solution transparency, the solution was poured into a tray and cooled to room temperature, leading to cellulose hydrogel formation. The cellulose hydrogel was washed thoroughly with deionized water. The washing process of 300 g (~170 ml) of cellulose gel containing 60 wt % LiBr consisted of 13 washing steps: twice with 100 ml of water for 24 hours each, once with 800 ml of water for 24 hours, and 10 times with 800 ml of water for 12 hours each. The final concentration of LiBr in the washed hydrogel was estimated to be about 1 part per billion, and the residual LiBr amount was confirmed by ICP-MS, as detailed in the "Characterization" section. Then, the washed hydrogel was sandwiched between metal plates with fold-back clips and subjected to drying at 70°C for 9 days. The dried hydrogel was rehydrated with water and subjected to press-drying at 110°C for 20 min under a pressure of 20 MPa by a heat press machine (AS ONE, Japan). The rationale for choosing these temperatures and pressure for processing is explained in figs. S18 and S19. Cup- or straw-shaped tPB was prepared by air-drying (at 70°C for 24 hours) a cup- or straw-shaped cellulose hydrogel that was prepared by a molding process (fig. S7). Energy consumption during processing was recorded with a watt checker (Sanwa Supply, Japan, TAP-TST8N). Coating of tPB with aluminum distearate was performed with an application of a

coating liquid containing 0.4 g of aluminum distearate, 20.0 g of cyclohexane, and 0.1 ml of ethanol, followed by air-drying.

Characterization

Trace element concentrations were analyzed by ICP-MS (iCAP Qc, Thermo Fisher Scientific, Waltham). The samples were cut into pieces of about 10 mg and cleaned by sonication with 8 mM HNO_3 for 5 min. Then, each sample was dried overnight at 65°C. Three milliliters of 68% HNO_3 (TAMAPURE-AA-100) was used to dissolve the samples at 120°C for about 60 hours. The element concentrations of cleaned samples were evaluated by triplicating each decomposition experiment. The supernatants were weighed into polypropylene vials and precleaned with HNO_3 and ultrapure water, and 0.3 M HNO_3 was added to each vial to make a 3-ml solution. The dilution rate was adjusted to about 30,000 times the initial sample weight. For instrument drift correction, Be, Sc, Y, and In were added to HNO_3 beforehand as internal standards. The following isotopes were used for detection: ^{7}Li, ^{23}Na, ^{25}Mg, ^{27}Al, ^{39}K, ^{44}Ca, ^{52}Cr, ^{55}Mn, ^{56}Fe, ^{59}Co, ^{60}Ni, ^{63}Cu, ^{66}Zn, ^{79}Br, ^{86}Sr, ^{107}Ag, ^{111}Cd, ^{138}Ba, and ^{208}Pb. To attenuate polyatomic/reactive interferences, H_2 was used as a cell gas for Fe and Li and He for the other elements. Optical properties were measured with a haze meter with a strong visible light source, illuminant C (HZ-V3, Suga Test Instruments Co., Ltd.), and UV-Vis V670 (JASCO Corp., Tokyo, Japan) equipped with a horizontal sampling integrating sphere unit (PIN-757). The three-point bending and wet tensile tests were performed on five specimens using an EZ-SX (Shimadzu Corp., Japan) equipped with a 500-N load cell. For three-point bending tests (the span and crosshead speed were 30 mm and 1%/min, respectively), the sample specimens were cuboid in shape with dimensions of 0.5 mm by 10 mm by 50 mm. ISO standards (e.g., ISO14125) specify that the thickness of the sample should be at least 2 mm. However, in this study, we were unable to prepare such a thick sample of tPB for mechanical testing. Therefore, we prepared tPB with a thickness of 0.5 mm and limited our discussion to the relative comparison of mechanical properties based on the three-point bending test results with PB and PC of the same thickness. For wet tensile tests (the span and crosshead speed were 40 mm and 1 mm/min, respectively), the sample specimens were cuboid in shape with dimensions of 0.5 mm by 5 mm by 60 mm and completely soaked in water for 72 hours before measurement. The bulk density was measured with a micrometrics powder pycnometer GeoPyc1365 (*70*), and the true density was measured with a MicrotracBEL helium gas pycnometer BELPycno (*71*). Micro–x-ray tomography was performed with ScanXmate-D160TSS105 (Comscantecno Co., Ltd., Kanagawa, Japan) with settings of 90 kV and 68 μA. AFM imaging was performed on a NaioAFM (Nanosurf, Switzerland). SEM imaging was performed on a Helios G4 UX (Thermo Fisher Scientific) equipped with a PP3010T cryogenic stage (Quorum Technologies Ltd.). For the SEM imaging of tPB, the tPB_{MCC} was mechanically fractured, and the surface and cross section were fixed on an aluminum stub using a carbon paste. SEM images without any conductive coatings were obtained at a landing voltage of 1 kV and a beam current of 6.3 pA. For the SEM imaging of undried cellulose hydrogel, the wet cellulose hydrogel was charged in a pair of through-hole brass rivets (inner diameter of 0.95 mm) and frozen in slush nitrogen (~−210°C). The paired rivets were mounted on an aluminum stub and vacuum transferred to the vacuum preparation chamber of the scanning electron microscope, in which the top rivet was fractured to expose the cross section, followed by water sublimation at −90°C for 3 min under ~2×10^{-3} Pa. The cross section was imaged at a landing voltage of 1 kV, a beam current of 6.3 pA, and a stage temperature of ~−150°C under ~3×10^{-5} Pa. A WAXD experiment was performed on Nanopix (Rigaku, Japan) at 40 kV and 30 mA with monochromatized and collimated Cu Kα radiation (λ = 1.548 Å). SAXS (λ = 1.0 Å) was conducted with synchrotron radiation at the BL40B2 beamline of Spring-8 (Hyogo, Japan). Thermal diffusivity was measured with a TA33 thermowave analyzer (Bethel Co., Ltd., Ibaraki, Japan) according to a previous method (*72*). Contact angle measurement was conducted by SImage Auto (Excimer Inc., Japan). Thermographic images were taken by TIM038V (AS ONE Corporation, Japan). M_w was measured by gel permeation chromatography (GPC) by using the Pullulan standard (STANDARD P-82, Shodex, Japan). The GPC system consisted of a GPC column packed with styrene divinylbenzene copolymer gel (GPC KD-806M, Shodex, Japan), a guard column (GPC KD-G4A, Shodex, Japan), and a refractive index detector (Waters2414, Waters, US). The mobile phase was 1.0% LiCl/DMAc, the flow rate was 0.8 ml/min, and the injected sample volume was 50 μl. The mobile phase was filtered with a polytetrafluoroethylene filter [06542-14, COSMONICE(R) Filter S, Nacalai Tesque, Japan]. The column temperature and the detector cell of the refractive index detector were set to 40°C. Data acquisition and processing were carried out using Empower2 software (Waters, US). Water retention test was performed gravimetrically. Water (100 g for cup-shaped tPB and 40 g for paper and polystyrene cup) was poured into the cups, and the time-course change in weight was recorded with AP135W (Shimadzu Corp., Japan).

Recycling

Solvent recycling was conducted by the condensation of wastewater containing 30 wt % LiBr at 160°C under nitrogen flow. The completion of condensation was confirmed by the density. The condensed solvent was filtered with activated carbon to remove the by-products generated during the dissolution process. Evaporated water was recovered in a cooled flask with an ice bath and used as washing water. Material recycling was performed by the pulverization of spent tPB and subsequent dissolution into the LiBr solvent.

Sample deployment and recovery

Environmental biodegradation tests were performed on the deep-sea floor at three sites: two bathyal sites [bathyal seafloor off the Misaki Peninsula, BMS (35°4.2′N, 139°32.5′E, at a water depth of 757 m from 12 May 2021 to 12 October 2021); bathyal hydrocarbon seepage off Hatsushima Island, BHT (35°0.9′N, 139°13.3′E, at a water depth of 855 m from 12 September 2019 to 7 January 2020 and from 5 February 2021 to 13 October 2021)] and one abyssal site [abyssal plain around Minamitorishima Island, AMN (22°59.9′N, 154°24.5′E, at a water depth of 5552 m from 15 March 2020 to 9 April 2021)] (fig. S14, A and B). As a reference site close to large cities and rivers, the same tests were performed in a coastal environment [port of JAMSTEC Yokosuka Headquarters PJM (35°19.2′N, 139°39.0′E, at a water depth of 2 m, from 8 August 2021 to 8 October 2021)]. The sample specimens were square in shape with dimensions of 0.2 to 0.6 mm by 30 mm by 30 mm, with the exception of AMN (1 mm by 5 mm by 30 mm). Five specimens were used at PJM, BHT, and BMS, and three specimens were used at AMN. The sample specimens used for on-site degradation tests at PJM, BHT, and BMS were sealed in mesh (fig. S14C). The mesh was stored in cylindrical

sample chambers (9 cm in diameter and 11.5 cm in height) with holes (98 holes, 8 mm in diameter) (fig. S14, D and E). The sample chambers were covered with protective nets and tagged with buoys (fig. S14F). The sample specimens used for on-site degradation tests at AMN were stored in centrifuge tubes with holes used as sample holders (fig. S14M). The sample holders were covered with protective nets (fig. S14N). Sample deployment (fig. S14J) and recovery (fig. S14, K and L) at deep-sea sites were conducted by a human-occupied vehicle (HOV) *Shinkai 6500* (fig. S14G) with R/V *Yokosuka* or remotely operated vehicles [*Hyper-Dolphin* (fig. S14H) with R/V *Shinsei-maru* and *KM-ROV* (fig. S14I) with R/V *Kaimei*]; AMN was an exception, where the free fall–type deep-sea observatory lander system *Edokko Mark 1* was used (fig. S14O). During sample recovery, the sample chambers were placed in a sample box with a lid until the HOV or ROV was recovered onboard to avoid the contamination of seawater in the upper layer (fig. S14L). Note that during recovery at AMN, the sample chambers fixed in the lander system went through the water column, leading to possible contamination. After recovery onboard, the sample chambers were readily dismounted, and one sample specimen was cut into pieces and subjected to fixation: freezing at −80°C for DNA/RNA extraction and fixation in 4% formaldehyde in 0.1 M phosphate buffer containing 150 mM NaCl (pH 7.4) for SEM observation. The remaining four (in PJM, BHT, and BMS) or two (in AMN) sample specimens were washed thoroughly with water, dried in an oven, and weighed. In addition, a cup-shaped tPB_{tex} was deployed and recovered at BHT (from 18 January 2022 to 5 June 2022).

SEM of degraded tPB

Sample-attached bacteria were fixed onboard as mentioned above. After washing with pure water, the fixed samples were dehydrated with a graded series of ethanol (30, 50, 70, 90, and 100%) for 10 min at room temperature and then substituted twice with *tert*-butyl alcohol. Consecutively, the samples were freeze dried and then sputter coated with gold using an MSP-1S magnetron sputter (Vacuum Device Inc., Japan) before examination using a JCM-7000 (JEOL, Japan) with a secondary electron detector with an acceleration voltage of 5 kV.

DNA and RNA coextraction and sequencing

The specimens of tPB were immediately placed on the shipboard at a temperature of −80°C and stored before nucleic acid extraction. Both DNA and RNA were coextracted using ZymoBIOMICS DNA/RNA Miniprep Kits (Zymo Research, Irvine, CA) according to the manufacturer's instructions. Briefly, the tPB sample was subjected to bead beating for 10 min at the maximum vortex speed (Vortex-Genie 2, Scientific Industries Inc., Bohemia, NY). The total nucleic acids were then separated into DNA and RNA by filtration. The metagenomic sequence library was constructed using the Illumina DNA Prep (M) Tagmentation kit (Illumina, San Diego, CA) with the Nextera DNA CD Index according to the manufacturer's instructions. The metatranscriptomic sequence library of total RNA in the microbial community was constructed by using a TruSeq Stranded mRNA Library Prep kit (Illumina, San Diego, CA) with a TruSeq RNA CD Index plate (Illumina, San Diego, CA) according to the manufacturer's instructions without a eukaryotic mRNA extraction step involving a polyA tail. Paired-end sequencing [150 base pairs (bp) × 2] was performed for both DNA and RNA libraries using the HiSeq X platform at Macrogen Japan.

Metagenomic assembly and functional annotation

The demultiplexed raw DNA and RNA sequence reads were quality trimmed by the trim read function with default parameters in CLC Genomic Workbench version 20.0 (QIAGEN, Venlo, The Netherlands). The 82,272,866 DNA reads were applied to the de novo assembly with scaffolding based on paired-end reads with *k*-nucleotide oligomers of 23 bp, bubble sizes of 800 bp, and minimum scaffold lengths of 400 bp on the CLC Genomics Workbench version 20.0 (QIAGEN, Venlo, The Netherlands) to obtain 190,979 scaffolds (the total base is 285,176,667 bp). The trimmed raw sequence reads were then mapped back to the 190,979 scaffolds for calculating the coverage of scaffolds using Map Reads and the contig function in CLC Genomics Workbench version 20.0 (QIAGEN) with length fractions of 0.7 and similarity fractions of 0.95. The 367,823 open reading frames (ORFs) were called from total scaffolds using MetaGeneMark (*73*). The taxonomic classification of each ORF was estimated by using GhostKOALA (*74*), and the estimated taxonomy of scaffolds was assigned on the basis of the most redundant taxonomic classification of ORFs coded in each scaffold, as described elsewhere (*75*). The Kyoto Encyclopedia of Genes and Genomes (KEGG) Automatic Annotation Server was used for KEGG orthology assignment with the single-directional best hit method set to 45 as the threshold assignment score (*76*). The gene encoding ribosomal protein S3 (rpsC, K02981), which is a key marker single-copy housekeeping gene for the phylogeny of microorganisms (*77*), was used for metagenome-based population analysis, as described previously (*78*). The dbCAN2 metaserver was used for the annotation of the carbohydrate-active enzyme (CaZy) by the default parameter of HMMER: dbCAN ($E < 1 \times 10^{-15}$; coverage >0.35) (*79*).

Extraction of the metagenome-assembled genome

Draft genomes [metagenome-assembled genomes (MAGs)] of highly abundant microorganisms within the biofilm community (coverage over 30) were extracted by grouping contigs using a coverage-GC% plot (*75*). The contig clusters were then refined by paired-end connections between contig ends that were counted by the Collect Paired Read Statistics function in the CLC Genome Finishing Module (QIAGEN), which allowed for the association of additional scaffolds and for the removal of incorrect scaffolds (*80*). To clarify the MAG quality proposed by the Genomic Standards Consortium (*81*), genome completeness and contamination were analyzed using CheckM, while the numbers of tRNAs and ribosomal RNAs per MAG were counted using tRNAscan-SE (*82*) and RNAmmer (*83*), respectively (table S5). To assign the taxonomic classification of the MAGs, GTDB-tk was run with default settings using the GTDB database release 95 (*84*).

Metatranscriptomic analysis

The 54,694,344 quality-trimmed RNA reads were mapped to the ORFs of the whole community by using the RNA sequencing analysis function of CLC Genomics Workbench version 20.0 (QIAGEN, Venlo, The Netherlands) at the default parameters, with the exception of the length fraction of 0.5 and the similarity fraction of 0.95. The RPKM (reads per kilobase per million mapped reads) values were calculated to analyze the gene expression levels of each coding sequence within the tPB microbiome (*85*). A heatmap was used to visualize the gene expression levels of the selected key metabolic genes among the dominant members of the community. The

selected key enzymes were as follows: endoglucanase (K01179) as cellulase mainly annotated as GH5 in CaZy, β-glucosidase (K05349), peroxidase (K03782) with CaZy annotation of AA2 (lignin peroxidase), and cellobiose phosphorylase (K00702) for cellulose degradation; glyceraldehyde 3-phosphate dehydrogenase (*gapA*, K00134) and enolase (*eno*, K01689) for glycolysis; average value of NADH-quinone oxidoreductase subunit A-L (*nuoA-L*, K00330-K00343), Na^+-transporting NADH:ubiquinone oxidoreductase subunit A-F (*nqrA-F*, K00346-00351), and cytochrome c oxidase (*coxA-C*, K02274-K002276) for aerobic respiration; flagellin (*fliC*, K02406) and pilin (*pilA*, K02650; *impB*, K11901) for swimming and microbial adhesion; F-type adenosine 5′-triphosphate (ATP) synthase (*atpA-H*, K02108-2115) and A-type ATP synthase (*ntpA-K*, K02117-K2124) for ATP synthesis; dissimilatory sulfite reductase (*dsrABC*, K11180, K11181, and K23077) for sulfate reduction; nitrogenase (*nifBDEHKN*, K02585-K02592) for nitrogen fixation and ammonium transporter (*amt*, K03320) for nitrogen source uptake; and formate dehydrogenase (*fdhAB*, K00123 and K00127), NiFe-hydrogenase (*hydAB*, K06281 and K06282), Fe-only hydrogenase (K00334-K00336), and D-lactate dehydrogenase (*ldhA*, K03778) for fermentation by-products and/or substrates. On the basis of these gene expression profiles for each MAG, the metabolic pathway within the community was estimated to analyze the degradation of cellulose-based tPB in the deep-sea environment.

LCA analysis

To estimate the greenhouse gas emissions associated with tPB production, we calculated the emissions on the basis of the energy consumption during tPB manufacturing under the assumption of ideal mass production (fig. S15). In this scenario, dissolving pulp was used as the starting material, and the LiBr and washing water used in the production process were assumed to be recycled within the system. Recycling was modeled through the condensation and separation of these components from the waste solution, using residual heat generated during cellulose dissolution and renewable energy. The calculations were performed using the Japanese database IDEA version 3.4 [developed by the National Institute of Advanced Industrial Science and Technology (AIST, Japan); https://riss.aist.go.jp/en-idealab/idea/]. Because of the usage restrictions of IDEA version 3.4, which prohibit the disclosure of original unit values from the database, a comparative analysis was conducted using relative values normalized to tPB as the reference.

Supplementary Materials

The PDF file includes:
Figs. S1 to S21
Tables S1 to S7
Legend for movie S1

Other Supplementary Material for this manuscript includes the following:
Movie S1

REFERENCES AND NOTES

1. J. R. Jambeck, R. Geyer, C. Wilcox, T. R. Siegler, M. Perryman, A. Andrady, R. Narayan, K. L. Law, Plastic waste inputs from land into the ocean. *Science* **347**, 768–771 (2015).
2. W. W. Y. Lau, Y. Shiran, R. M. Bailey, E. Cook, M. R. Stuchtey, J. Koskella, C. A. Velis, L. Godfrey, J. Boucher, M. B. Murphy, R. C. Thompson, E. Jankowska, A. Castillo Castillo, T. D. Pilditch, B. Dixon, L. Koerselman, E. Kosior, E. Favoino, J. Gutberlet, S. Baulch, M. E. Atreya, D. Fischer, K. K. He, M. M. Petit, U. R. Sumaila, E. Neil, M. V. Bernhofen, K. Lawrence, J. E. Palardy, Evaluating scenarios toward zero plastic pollution. *Science* **369**, 1455–1461 (2020).
3. L. J. J. Meijer, T. van Emmerik, R. van der Ent, C. Schmidt, L. Lebreton, More than 1000 rivers account for 80% of global riverine plastic emissions into the ocean. *Sci. Adv.* **7**, eaaz5803 (2021).
4. Estimates of global marine plastic mass demystify the missing plastic paradox. *Nat. Geosci.* **16**, 665–666 (2023).
5. C. Morales-Caselles, J. Viejo, E. Martí, D. González-Fernández, H. Pragnell-Raasch, J. I. González-Gordillo, E. Montero, G. M. Arroyo, G. Hanke, V. S. Salvo, O. C. Basurko, N. Mallos, L. Lebreton, F. Echevarría, T. van Emmerik, C. M. Duarte, J. A. Gálvez, E. van Sebille, F. Galgani, C. M. García, P. S. Ross, A. Bartual, C. Ioakeimidis, G. Markalain, A. Isobe, A. Cózar, An inshore–offshore sorting system revealed from global classification of ocean litter. *Nat. Sustain.* **4**, 484–493 (2021).
6. M. Egger, F. Sulu-Gambari, L. Lebreton, First evidence of plastic fallout from the North Pacific Garbage Patch. *Sci. Rep.* **10**, 7495 (2020).
7. R. Nakajima, M. Tsuchiya, A. Yabuki, S. Masuda, T. Kitahashi, Y. Nagano, T. Ikuta, N. Isobe, H. Nakata, H. Ritchie, K. Oguri, S. Osafune, K. Kawamura, M. Suzukawa, T. Yamauchi, K. Iijima, T. Yoshida, S. Chiba, K. Fujikura, Massive occurrence of benthic plastic debris at the abyssal seafloor beneath the Kuroshio Extension, the North West Pacific. *Mar. Pollut. Bull.* **166**, 112188 (2021).
8. UNEP, "What you need to know about the plastic pollution resolution" (2022); www.unep.org/news-and-stories/story/what-you-need-know-about-plastic-pollution-resolution.
9. UNEP, "Single-use plastic: A roadmap for sustainability" (2018); www.unep.org/resources/report/single-use-plastics-roadmap-sustainability.
10. R. Nakajima, T. Miyama, T. Kitahashi, N. Isobe, Y. Nagano, T. Ikuta, K. Oguri, M. Tsuchiya, T. Yoshida, K. Aoki, Y. Maeda, K. Kawamura, M. Suzukawa, T. Yamauchi, H. Ritchie, K. Fujikura, A. Yabuki, Plastic after an extreme storm: The typhoon-induced response of micro- and mesoplastics in Coastal waters. *Front. Mar. Sci.* **8**, 806952 (2022).
11. On the plastics crisis. *Nat. Sustain.* **6**, 1137 (2023).
12. G. L. Robertson, *Food Packaging: Principles and Practice* (CRC Press, ed. 3, 2012).
13. World Economic Forum, Ellen MacArthur Foundation and McKinsey & Company, *The New Plastics Economy: Rethinking the Future of Plastics* (Ellen MacArthur Foundation, 2016).
14. M.-C. Hsieh, H. Koga, K. Suganuma, M. Nogi, Hazy transparent cellulose nanopaper. *Sci. Rep.* **7**, 41590 (2017).
15. G. Simmonds, A. T. Woods, C. Spence, 'Show me the goods': Assessing the effectiveness of transparent packaging vs. product imagery on product evaluation. *Food Qual. Prefer.* **63**, 18–27 (2018).
16. L. Girard, "PepsiCo passe du carton au plastique pour emballer ses jus Tropicana," ["PepsiCo is switching from paperboard to plastic for packaging its Tropicana juices."] *Le Monde*, 12 June 2019; www.lemonde.fr/economie/article/2019/06/12/pepsico-passe-du-carton-au-plastique-pour-emballer-ses-jus-tropicana_5475211_3234.html.
17. C. F. Cross, E. J. Bevan, C. Beadle, Method of treating viscose and products derived therefrom US Patent US717355A (1901).
18. G. Kauffman, Eduard Schweizer (1818-1860): The unknown chemist and his well-known reagent. *J. Chem. Educ.* **61**, 1095 (1984).
19. I. Miyamoto, M. Inamoto, T. Matsui, M. Saito, K. Okajima, Studies on structure of cuprammonium cellulose I. A circular dichroism study on the dissolved state of cellulose in cuprammonium solution. *Polym. J.* **27**, 1113–1122 (1995).
20. H.-P. Fink, P. Weigel, H. J. Purz, J. Ganster, Structure formation of regenerated cellulose materials from NMMO-solutions. *Prog. Polym. Sci.* **26**, 1473–1524 (2001).
21. A. Michud, M. Tanttu, S. Asaadi, Y. Ma, E. Netti, P. Käärainen, A. Persson, A. Berntsson, M. Hummel, H. Sixta, Ioncell-F: Ionic liquid-based cellulosic textile fibers as an alternative to viscose and Lyocell. *Text. Res. J.* **86**, 543–552 (2016).
22. Y.-J. Yang, J.-M. Shin, T. H. Kang, S. Kimura, M. Wada, U.-J. Kim, Cellulose dissolution in aqueous lithium bromide solutions. *Cellulose* **21**, 1175–1181 (2014).
23. N. Isobe, T. Komamiya, S. Kimura, U.-J. Kim, M. Wada, Cellulose hydrogel with tunable shape and mechanical properties: From rigid cylinder to soft scaffold. *Int. J. Biol. Macromol.* **117**, 625–631 (2018).
24. S.-C. Yang, Y. Liao, K. G. Karthikeyan, X. J. Pan, Mesoporous cellulose-chitosan composite hydrogel fabricated via the co-dissolution-regeneration process as biosorbent of heavy metals. *Environ. Pollut.* **286**, 117324 (2021).
25. M. Nogi, S. Iwamoto, A. N. Nakagaito, H. Yano, Optically transparent nanofiber paper. *Adv. Mater.* **21**, 1595–1598 (2009).
26. N. Soykeabkaew, C. Sian, S. Gea, T. Nishino, T. Peijs, All-cellulose nanocomposites by surface selective dissolution of bacterial cellulose. *Cellulose* **16**, 435–444 (2009).
27. H. Yousefi, T. Nishino, M. Faezipour, G. Ebrahimi, A. Shakeri, Direct fabrication of *all*-cellulose nanocomposite from cellulose microfibers using ionic liquid-based nanowelding. *Biomacromolecules* **12**, 4080–4085 (2011).
28. F. Mayer, A. Prado-Roller, A. Mautner, A. Bismarck, Retain strength, gain ductility: Tough and transparent nanopapers by mercerisation. *Cellulose* **31**, 1533–1544 (2024).

29. D. Wloch, N. Herrera, K.-Y. Lee, Optically transparent laminated acrylic composites reinforced with mercerised bacterial cellulose nanopaper. *Compos. Part A Appl. Sci. Manuf.* **172**, 107583 (2023).
30. N. Isobe, M. Sekine, S. Kimura, M. Wada, S. Kuga, Anomalous reinforcing effects in cellulose gel-based polymeric nanocomposites. *Cellulose* **18**, 327–333 (2011).
31. S. Ide, Filter made of cuprammonium regenerated cellulose for virus removal: A mini-review. *Cellulose* **29**, 2779–2793 (2022).
32. H. Chen, A. Baitenov, Y. Li, E. Vasileva, S. Popov, I. Sychugov, M. Yan, L. Berglund, Thickness dependence of optical transmittance of transparent wood: Chemical modification effects. *ACS Appl. Mater. Interfaces* **11**, 35451–35457 (2019).
33. W. Sakuma, S. Fujisawa, L. A. Berglund, T. Saito, Nanocellulose xerogel as template for transparent, thick, flame-retardant polymer nanocomposites. *Nanomaterials* **11**, 3032 (2021).
34. H. Fukuzumi, T. Saito, T. Iwata, Y. Kumamoto, A. Isogai, Transparent and high gas barrier films of cellulose nanofibers prepared by TEMPO-mediated oxidation. *Biomacromolecules* **10**, 162–165 (2009).
35. T. Kasuga, N. Isobe, H. Yagyu, H. Koga, M. Nogi, Clearly transparent nanopaper from highly concentrated cellulose nanofiber dispersion using dilution and sonication. *Nanomaterials* **8**, 104 (2018).
36. S. Ishioka, N. Isobe, T. Hirano, N. Matoba, S. Fujisawa, T. Saito, Fully wood-based transparent plates with high strength, flame self-extinction, and anisotropic thermal conduction. *ACS Sustain. Chem. Eng.* **11**, 2440–2448 (2023).
37. T. Neubert, W. Sun, F. Neumann, M. Vergoehl, "Characterization of photocatalytic activity of TiO_2 thin films for optical applications," in *Optical Interference Coatings* (OSA, 2007), p. ThA10; https://opg.optica.org/abstract.cfm?uri=OIC-2007-ThA10.
38. A. Walther, F. Lossada, T. Benselfelt, K. Kriechbaum, L. Berglund, O. Ikkala, T. Saito, L. Wågberg, L. Bergström, Best practice for reporting wet mechanical properties of nanocellulose-based materials. *Biomacromolecules* **21**, 2536–2540 (2020).
39. J. Zhou, L. Zhang, Solubility of cellulose in NaOH/Urea aqueous solution. *Polym. J.* **32**, 866–870 (2000).
40. L. K. Tolonen, G. Zuckerstätter, P. A. Penttilä, W. Milacher, W. Habicht, R. Serimaa, A. Kruse, H. Sixta, Structural changes in microcrystalline cellulose in subcritical water treatment. *Biomacromolecules* **12**, 2544–2551 (2011).
41. R. L. Whistler, D. F. Durso, Chromatographic separation of sugars on charcoal. *J. Am. Chem. Soc.* **72**, 677–679 (1950).
42. T. Omura, N. Isobe, T. Miura, S. Ishii, M. Mori, Y. Ishitani, S. Kimura, K. Hidaka, K. Komiyama, M. Suzuki, K.-I. Kasuya, H. Nomaki, R. Nakajima, M. Tsuchiya, S. Kawagucci, H. Mori, A. Nakayama, M. Kunioka, K. Kamino, T. Iwata, Microbial decomposition of biodegradable plastics on the deep-sea floor. *Nat. Commun.* **15**, 568 (2024).
43. T. Nagata, C. Tamburini, J. Arístegui, F. Baltar, A. B. Bochdansky, S. Fonda-Umani, H. Fukuda, A. Gogou, D. A. Hansell, R. L. Hansman, G. J. Herndl, C. Panagiotopoulos, T. Reinthaler, R. Sohrin, P. Verdugo, N. Yamada, Y. Yamashita, T. Yokokawa, D. H. Bartlett, Emerging concepts on microbial processes in the bathypelagic ocean–Ecology, biogeochemistry, and genomics. *Deep. Res. Part II Top. Stud. Oceanogr.* **57**, 1519–1536 (2010).
44. L. J. Nilsson, E. D. Larson, K. R. Gilbreath, A. Gupta, "Energy efficiency and the pulp and paper industry" (1995).
45. X. Zhang, N. Xiao, H. Wang, C. Liu, X. Pan, Preparation and characterization of regenerated cellulose film from a solution in lithium bromide molten salt hydrate. *Polymers* **10**, 614 (2018).
46. J. Yang, G.-J. Kwon, K. Hwang, D.-Y. Kim, Cellulose–chitosan antibacterial composite films prepared from LiBr solution. *Polymers* **10**, 1058 (2018).
47. H. J. Kim, Y. J. Yang, H. J. Oh, S. Kimura, M. Wada, U.-J. Kim, Cellulose–silk fibroin hydrogels prepared in a lithium bromide aqueous solution. *Cellulose* **24**, 5079–5088 (2017).
48. U.-J. Kim, D. Kim, J. You, J. W. Choi, S. Kimura, M. Wada, Preparation of cellulose-chitosan foams using an aqueous lithium bromide solution and their adsorption ability for Congo red. *Cellulose* **25**, 2615–2628 (2018).
49. Y. Liao, Z. Pang, X. Pan, Fabrication and mechanistic study of aerogels directly from whole biomass. *ACS Sustain. Chem. Eng.* **7**, 17723–17736 (2019).
50. U.-J. Kim, S. Kimura, M. Wada, Facile preparation of cellulose-SiO_2 composite aerogels with high SiO_2 contents using a LiBr aqueous solution. *Carbohydr. Polym.* **222**, 114975 (2019).
51. L. Zhang, Y. Liao, Y.-C. Wang, S. Zhang, W. Yang, X. Pan, Z. L. Wang, Cellulose II aerogel-based triboelectric nanogenerator. *Adv. Funct. Mater.* **30**, 2001763 (2020).
52. Y. Liao, X. Pan, Self-indicating and high-capacity mesoporous aerogel-based biosorbent fabricated from cellulose and chitosan via co-dissolution and regeneration for removing formaldehyde from indoor air. *Environ. Sci. Nano* **8**, 1283–1295 (2021).
53. P. Srikhirin, S. Aphornratana, S. Chungpaibulpatana, A review of absorption refrigeration technologies. *Renew. Sustain. Energy Rev.* **5**, 343–372 (2001).
54. K. D. Rafferty, "Absorption refrigeration," in *GHC Bulletin* (1998), pp. 33–36.
55. F. Liu, J. Sui, T. Liu, H. Jin, Performance investigation of a combined heat pump transformer operating with water/lithium bromide. *Energ. Conver. Manage.* **140**, 295–306 (2017).
56. C. Somers, A. Mortazavi, Y. Hwang, R. Radermacher, P. Rodgers, S. Al-Hashimi, Modeling water/lithium bromide absorption chillers in ASPEN Plus. *Appl. Energy* **88**, 4197–4205 (2011).
57. W. Pei, Q. Cheng, S. Jiao, L. Liu, Performance evaluation of the electrodialysis regenerator for the lithium bromide solution with high concentration in the liquid desiccant air-conditioning system. *Energy* **187**, 115928 (2019).
58. Z. Wang, Z. Gu, S. Feng, Y. Li, Application of vacuum membrane distillation to lithium bromide absorption refrigeration system. *Int. J. Refrig.* **32**, 1587–1596 (2009).
59. A. Pongtornkulpanich, S. Thepa, M. Amornkitbamrung, C. Butcher, Experience with fully operational solar-driven 10-ton $LiBr/H_2O$ single-effect absorption cooling system in Thailand. *Renew. Energy* **33**, 943–949 (2008).
60. F. P. La Mantia, "Basic concepts on the recycling of homogeneous and heterogeneous plastics," in *Recycling of PVC and Mixed Plastic Waste*, F. P. La Mantia, Ed. (ChemTec Publishing, 1996), pp. 63–76.
61. R. Nagamine, K. Kobayashi, R. Kusumi, M. Wada, Cellulose fiber biodegradation in natural waters: River water, brackish water, and seawater. *Cellul.* **29**, 2917–2926 (2022).
62. I. E. Napper, R. C. Thompson, Environmental deterioration of biodegradable, oxo-biodegradable, compostable, and conventional plastic carrier bags in the sea, soil, and open-air over a 3-year period. *Environ. Sci. Technol.* **53**, 4775–4783 (2019).
63. T. P. Haider, C. Völker, J. Kramm, K. Landfester, F. R. Wurm, Plastics of the future? The impact of biodegradable polymers on the environment and on society. *Angew. Chemie Int. Ed. Engl.* **58**, 50–62 (2019).
64. N. B. Erdal, M. Hakkarainen, Degradation of cellulose derivatives in laboratory, man-made, and natural environments. *Biomacromolecules* **23**, 2713–2729 (2022).
65. V. Grossi, P. Blokker, J. S. Sinninghe Damsté, Anaerobic biodegradation of lipids of the marine microalga *Nannochloropsis salina*. *Org. Geochem.* **32**, 795–808 (2001).
66. J. Tria, E. C. V. Butler, P. R. Haddad, A. R. Bowie, Determination of aluminium in natural water samples. *Anal. Chim. Acta* **588**, 153–165 (2007).
67. H. B. Maring, R. A. Duce, The impact of atmospheric aerosols on trace metal chemistry in open ocean surface seawater, 1. Aluminum. *Earth Planet. Sci. Lett.* **84**, 381–392 (1987).
68. K. Li, S. Wang, H. Chen, X. Yang, L. A. Berglund, Q. Zhou, Self-densification of highly mesoporous wood structure into a strong and transparent film. *Adv. Mater.* **32**, 2003653 (2020).
69. M. Zhu, Y. Wang, S. Zhu, L. Xu, C. Jia, J. Dai, J. Song, Y. Yao, Y. Wang, Y. Li, D. Henderson, W. Luo, H. Li, M. L. Minus, T. Li, L. Hu, Anisotropic, transparent films with aligned cellulose nanofibers. *Adv. Mater.* **29**, 1606284 (2017).
70. W. Sakuma, S. Yamasaki, S. Fujisawa, T. Kodama, J. Shiomi, K. Kanamori, T. Saito, Mechanically strong, scalable, mesoporous xerogels of nanocellulose featuring light permeability, thermal insulation, and flame self-extinction. *ACS Nano* **15**, 1436–1444 (2021).
71. K. Daicho, K. Kobayashi, S. Fujisawa, T. Saito, Crystallinity-independent yet modification-dependent true density of nanocellulose. *Biomacromolecules* **21**, 939–945 (2020).
72. K. Uetani, T. Okada, H. T. Oyama, Crystallite size effect on thermal conductive properties of nonwoven nanocellulose sheets. *Biomacromolecules* **16**, 2220–2227 (2015).
73. W. Zhu, A. Lomsadze, M. Borodovsky, Ab initio gene identification in metagenomic sequences. *Nucleic Acids Res.* **38**, e132 (2010).
74. M. Kanehisa, Y. Sato, K. Morishima, BlastKOALA and GhostKOALA: KEGG tools for functional characterization of genome and metagenome sequences. *J. Mol. Biol.* **428**, 726–731 (2016).
75. S. Ishii, S. Suzuki, T. M. Norden-Krichmar, A. Tenney, P. S. G. Chain, M. B. Scholz, K. H. Nealson, O. Bretschger, A novel metatranscriptomic approach to identify gene expression dynamics during extracellular electron transfer. *Nat. Commun.* **4**, 1601 (2013).
76. Y. Moriya, M. Itoh, S. Okuda, A. C. Yoshizawa, M. Kanehisa, KAAS: An automatic genome annotation and pathway reconstruction server. *Nucleic Acids Res.* **35**, 182–185 (2007).
77. C. T. Brown, L. A. Hug, B. C. Thomas, I. Sharon, C. J. Castelle, A. Singh, M. J. Wilkins, K. C. Wrighton, K. H. Williams, J. F. Banfield, Unusual biology across a group comprising more than 15% of domain bacteria. *Nature* **523**, 208–211 (2015).
78. S. Ishii, S. Suzuki, A. Tenney, K. H. Nealson, O. Bretschger, Comparative metatranscriptomics reveals extracellular electron transfer pathways conferring microbial adaptivity to surface redox potential changes. *ISME J.* **12**, 2844–2863 (2018).
79. H. Zhang, T. Yohe, L. Huang, S. Entwistle, P. Wu, Z. Yang, P. K. Busk, Y. Xu, Y. Yin, DbCAN2: A meta server for automated carbohydrate-active enzyme annotation. *Nucleic Acids Res.* **46**, W95–W101 (2018).
80. M. Albertsen, P. Hugenholtz, A. Skarshewski, K. L. Nielsen, G. W. Tyson, P. H. Nielsen, Genome sequences of rare, uncultured bacteria obtained by differential coverage binning of multiple metagenomes. *Nat. Biotechnol.* **31**, 533–538 (2013).
81. R. M. Bowers, N. C. Kyrpides, R. Stepanauskas, M. Harmon-Smith, D. Doud, T. B. K. Reddy, F. Schulz, J. Jarett, A. R. Rivers, E. A. Eloe-Fadrosh, S. G. Tringe, N. N. Ivanova, A. Copeland, A. Clum, E. D. Becraft, R. R. Malmstrom, B. Birren, M. Podar, P. Bork, G. M. Weinstock, G. M. Garrity, J. A. Dodsworth, S. Yooseph, G. Sutton, F. O. Glöckner, J. A. Gilbert, W. C. Nelson, S. J. Hallam, S. P. Jungbluth, T. J. G. Ettema, S. Tighe, K. T. Konstantinidis, W. T. Liu, B. J. Baker, T. Rattei, J. A. Eisen, B. Hedlund, K. D. McMahon, N. Fierer, R. Knight,

R. Finn, G. Cochrane, I. Karsch-Mizrachi, G. W. Tyson, C. Rinke, A. Lapidus, F. Meyer, P. Yilmaz, D. H. Parks, A. M. Eren, L. Schriml, J. F. Banfield, P. Hugenholtz, T. Woyke, Minimum information about a single amplified genome (MISAG) and a metagenome-assembled genome (MIMAG) of bacteria and archaea. *Nat. Biotechnol.* **35**, 725–731 (2017).
82. T. M. Lowe, S. R. Eddy, TRNAscan-SE: A program for improved detection of transfer RNA genes in genomic sequence. *Nucleic Acids Res.* **25**, 955–964 (1996).
83. K. Lagesen, P. Hallin, E. A. Rødland, H. H. Stærfeldt, T. Rognes, D. W. Ussery, RNAmmer: Consistent and rapid annotation of ribosomal RNA genes. *Nucleic Acids Res.* **35**, 3100–3108 (2007).
84. P. A. Chaumeil, A. J. Mussig, P. Hugenholtz, D. H. Parks, GTDB-Tk: A toolkit to classify genomes with the genome taxonomy database. *Bioinformatics* **36**, 1925–1927 (2020).
85. A. Mortazavi, B. A. Williams, K. McCue, L. Schaeffer, B. Wold, Mapping and quantifying mammalian transcriptomes by RNA-Seq. *Nat. Methods* **5**, 621–628 (2008).
86. R. Berggren, F. Berthold, E. Sjöholm, M. Lindström, Improved methods for evaluating the molar mass distributions of cellulose in kraft pulp. *J. Appl. Polym. Sci.* **88**, 1170–1179 (2003).
87. J. Laurijssen, A. Faaij, E. Worrell, Benchmarking energy use in the paper industry: A bench marking study on process unit level. *Energy Effic.* **6**, 49–63 (2013).

Acknowledgments: We thank the captain and crew of R/Vs *Yokosuka*, *Kairei*, *Shinsei-maru*, and *Kaimei* for great support of scientific activity during the expeditions YK19-11 (Principal investigator: A. Yabuki), YK21-08C, YK21-18C, KR20-E01C, KR21-04C, KS-20-1, KM20-09, and KM21-E02. We extend thanks to the HOV *Shinkai 6500* team, ROV *Hyper-Dolphin* team, and ROV *KM-ROV* team. We acknowledge S. Matsugaura and T. Miwa (JAMSTEC) for providing advice and support during *Edokko Mark 1* deployment. We thank S. Suzuki, Y. Sakao, and T. Fukumi for technical assistance in DNA and RNA extraction and sequence library preparation at JAMSTEC. We also thank C. Chen (JAMSTEC) for constructive comments on the manuscript. **Funding:** N.I. acknowledges support from the Grants-in-Aid for Scientific Research (KAKENHI grant nos. JP22H03786 and JP22K19885) from the Japan Society for the Promotion of Science (JSPS). T.S. acknowledges support from CREST project (grant number JPMJCR22L3) from the Japan Science and Technology Agency (JST). This paper was based on the results obtained from a project, JPNP18016 and PJ-ID 20001845, commissioned by the New Energy and Industrial Technology Development Organization (NEDO). The synchrotron radiation experiments were performed at SPring-8 (proposal no. 2021B1682) at BL40B2. A part of this work was supported by Council for Science, Technology and Innovation (CSTI), Cross-ministerial Strategic Innovation Promotion Program (SIP), "Innovative Technology for Exploration of Deep Sea Resources" (lead agency: JAMSTEC). **Author contributions:** N.I. conceived the concept and designed the study. N.I., K.T., and Y.S. prepared the sample specimens. ICP-MS was performed by T.Y. and analyzed by N.I and T.Y. Optical measurements were performed and analyzed by N.I and W.S. Bending and tensile tests were performed and analyzed by N.I and K.T. SEM was performed by S.O and S.Ki. and analyzed by N.I., S.O., and S.Ki. Micro–x-ray tomography was performed by K.K. and analyzed by S.O and N.I. Density measurements were performed by D.K. and W.S. and analyzed by N.I., D.K., and W.S. Thermal diffusivity was measured and analyzed by K.U. Metagenomic analyses were performed by S.I. On-site degradation tests were performed by N.I., K.T., Y.S., S.Ki, R.N., M.T., T.Ik., S.Ka., T.Iw., and H.N. N.I and S.I. cowrote the manuscript. N.I., S.I., S.O., K.D., W.S., K.U., T.S., R.N., M.T., T.Ik., S.Ka, T.Iw., and H.N. revised the manuscript. N.I., K.T., S.I., Y.S., S.O., K.D., W.S., K.U., T.Y., K.K., S.Ki., T.S., R.N., M.T., T.Ik., S.Ka., T.Iw., and H.N. commented on the submitted version of the manuscript. **Competing interests:** The authors declare that they have no competing interests. **Data and materials availability:** All data needed to evaluate the conclusion in the paper are present in the paper and/or the Supplementary Materials. All sequence reads, assembled scaffolds, and genomic sequences of the eight MAGs were deposited to GenBank in BioProject PRJNA883034. The raw sequence reads of the tPB_BHT04 microbiome were deposited to GenBank Sequence Read Archive under accession numbers SRR21695763 for DNA and SRR21695762 for RNA, while the assembled scaffolds of the tPB_BHT04 metagenome were deposited and the assembled contigs have been deposited in DDBJ/EMBL/GenBank under accession number JAOPTP000000000. The eight MAGs were separately deposited to GenBank with PGAP annotation under accession numbers JAOPTX000000000 for tPB_Fibr1, JAOPTW000000000 for tPB_Fibr2, JAOPTV000000000 for tPB_Delt1, JAOPTU000000000 for tPB_Delt2, JAOPTT000000000 for tPB_Spir1, JAOPTS000000000 for tPB_Bact1, JAOPTR000000000 for tPB_Alph1, and JAOPTQ000000000 for tPB_Gamm1. Source data are provided with this paper.

Submitted 4 August 2024
Accepted 4 March 2025
Published 9 April 2025
10.1126/sciadv.ads2426